Highly-dense Acrylonitrile Butadiene Styrene Specimens Fabricated by Overheat Fused Filament Fabrication Printing

Thang Q. Tran, Xinying Deng, Carla Canturri, Chu Long Tham, Feng Lin Ng

Singapore Institute of Manufacturing Technology, 73 Nanyang Drive, 637662, Singapore

Abstract

Purpose – This study aims to comprehensively investigate the process-structure-property correlation of ABS parts manufactured by the overheat fused filament fabrication (FFF) method. The study considers the relationships between the tensile and impact strength with temperature profiles, mesostructures, and fracture behaviors of the ABS printed parts.

Design/methodology/approach – The overheat printing condition was generated by employing the highest possible printing temperature of the FFF printer used in this study together with cooling fan turned off. Temperature profiles of the polymer rasters were measured to characterize the diffusion time of the deposited rasters. Thermogravimetric analysis (TGA), differential scanning calorimetry (DSC), and melt flow index (MFI) were performed to study the thermal properties of the ABS feedstock. The mesostructures of the printed ABS samples were characterized by employing an optical microscope, while their fracture surface was investigated using a field emission scanning electron microscope. The authors performed the tensile and impact tests following ASTM D3039 and D256-10A, respectively.

Findings – The use of the overheat FFF printing could offer better raster diffusion with reduced cooling rate and prolonged diffusion time. Consequently, the overheat printed ABS parts possessed a porosity as low as 1.35% with an increase in the weld length formed between the adjacent rasters of up to 62.5%. More importantly, the overheat printed ABS parts exhibited an increase of up to 70%, 84%, and 30% in tensile strain at break, tensile toughness, and impact strength, respectively, compared to their normal printed counterparts.

Originality/value – This research provides a facile but effective approach to fabricate highly-dense and strong polymeric parts printed by FFF method for end-use applications.

Keywords Additive manufacturing, Fused filament fabrication, 3D printing, overheat printing, tensile strength, impact strength, acrylonitrile butadiene styrene.

1. Introduction

In the recent years, additive manufacturing (AM), also known as 3D printing, has been growing rapidly due to their outstanding advantages such as ability to fabricate geometrically complicated parts with precise dimensions, high customization, low waste production, and short lead time (Khorasani *et al.*, 2022). By adding material layer-by-layer based on CAD models, complex 3D parts made of metals, polymers, ceramics, and composites can be fabricated for a wide range of applications such as automobiles (Wiese *et al.*, 2020), aerospace (Ahmed and Page, 2013), medical applications (Lathers and La Belle, 2017), electronics (Zhang *et al.*, 2020), textile (Grimmelsmann *et al.*, 2018), and machinery (Tran *et al.*, 2019). Among the AM techniques for polymers, fused filament fabrication (FFF) or fused deposition modeling (FDM) is one of the most widely used AM methods to process thermoplastics thanks to its simple process, high cost-effectiveness, and economic accessibility (Tran *et al.*, 2022b).

Similar to other AM processes, FFF technique has tendency to generate pores and voids in the structure of the printed parts, especially those formed between the elliptical or oval-shaped polymer rasters (Wang *et al.*, 2019). These voids are the result of the fast cooling rate of the extruded melt material during the printing process. When the melt material is deposited on the underlying cold layer, its temperature reduces rapidly, leading to poor diffusion between the adjacent rasters. Consequently, the growth of neck formed between the rasters is incomplete, resulting in the formation of inter-raster voids (Abbott *et al.*, 2018; Sun *et al.*, 2008). Notably, the estimated void fraction or porosity of the FFF printed parts is between 6% and 22%, depending on the printing processes and material feedstocks used (Böhler *et al.*, 2020; Majid *et al.*, 2017). Void defect is one of the critical issues of the FFF process that lower the mechanical performance of the printed components and, therefore, limit their practical applications to mainly conceptual prototyping (Wang *et al.*, 2019).

Over the last decade, many methods have been developed to reduce the porosity and enhance the mechanical performance of the FFF printed parts (Tran *et al.*, 2022b). They can be classified into 4 main approaches: process optimization (Tran *et al.*, 2022a), feedstock modification (Wang *et al.*, 2016), process modification (Böhler *et al.*, 2020), and post-treatments (Jo *et al.*, 2018). Among these methods, process optimization is the most facile and cost-effective approach as there are no requirements for expensive and complicated modification of the feedstock materials and equipment or additional time-consuming post-treatment steps. In fact, this method only requires the optimization of some important process parameters such as infill density, air gap, raster angle, extrusion flowrate, printing temperature, cooling fan speed, and layer thickness to achieve specific required properties. More importantly, it is also one of the most effective methods to decrease the porosity of the FFF printed parts, resulting in comparable parts' mechanical performance to those fabricated by conventional manufacturing methods (Schirmeister *et al.*, 2019).

Among the aforementioned process parameters, printing temperature and cooling fan speed are the crucial factors that determine the cooling rate of the extruded polymer melt and, hence, the porosity of the FFF printed parts. Although several studies have shown that high printing temperature and low cooling fan speed could improve the structure and tensile strength of the FFF printed parts (Kuznetsov *et al.*, 2020), the effects of overheat FFF printing with substantially high printing temperature and no usage of cooling fan on the mechanical performance of the printed neat polymer parts have not been investigated. Additionally, while many research work on FFF in literature only reported the used process parameters and their resulting printed parts' properties (Kuo *et al.*, 2021), studies on relationships between these factors with the thermal profiles of polymer rasters as well as the mesostructures and fracture behaviors of the printed parts are still very limited (Tran *et al.*, 2022a). Research on such comprehensive process-structure-property correlation could provide insights into the optimization of crucial process parameters to fabricate components with desired structures and performance.

In this paper, we aim to fabricate highly dense acrylonitrile butadiene styrene (ABS) specimens by using an overheat FFF process. The overheat printing was conducted by employing the highest possible printing temperature of the FFF printer used in this study together with cooling fan turned off to minimize the cooling rate of the extruded ABS melt during the printing process. Moreover, influences of the overheat printing on tensile and impact strength of the ABS printed parts were discussed while their relationships with temperature profiles, mesostructures, and fracture behaviors were investigated. The results show that the overheat FFF printing could be a promising technique to fabricate reliable and high-performance printed ABS specimens with low porosity.

2. Experimental section

2.1 Materials

Raise3D Premium ABS filament was used throughout this study. For the mounting of loading tabs for the tensile specimens Araldite® 2000 adhesive and Norplex NP500A glass fiber composite tabs were used.

2.2 FFF printing of ABS specimens

FFF printing of ABS specimens was performed on a Raise3D Pro2 printer equipped with a 0.4-mm-diameter nozzle. ideaMaker 3.4.2 software was employed to generate G-code files required for the printer based on CAD models. Table 1 presents the essential printing parameters of the normal and overheat FFF processes conducted in this study. As can be seen, the normal FFF process used the printing parameters of ABS template settings in the ideaMaker slicer, which were recommended by Raise3D manufacturer. The printer was equipped with a heated build plate to minimize warpage issues during the printing process. A 1.82-mm-thick raft was printed below the printed polymer parts to improve their adhesion with the build plate. Only infill angles of [45°/-45°] and [0°/90°] were employed in this study as they are the most widely used bidirectional raster configurations. Infill overlap was set at 5% to provide good bonding between the infill and shell of the printed parts. While most of the printing parameters in the overheat FFF process were similar to those in the normal process, its printing temperature was the highest possible offered by the used printer (310 ^{o}C) and the cooling fan was turned off to generate the overheat condition during the printing process.

Table I. Important printing parameters of ABS used in the normal and overheat processes.

Parameter	Normal FFF process	Overheat FFF process
Printing temperature	250 ^{o}C	310 ^{o}C
Build plate temperature	110 ^{o}C	110 ^{o}C
Cooling fan speed	50%	0%
Printing speed	60 mm/s	60 mm/s
Layer thickness	0.25 mm	0.25 mm
Raster width (mm)	0.4 mm	0.4 mm
Shell number	2	2
Infill Density	100%	100%
Infill overlap	5%	5%
Fill pattern	Lines	Lines
Infill angle	[45°/-45°] and [0°/90°]	[45°/-45°] and [0°/90°]
Raft thickness	1.82 mm	1.82 mm

2.3 Temperature profile measurement

To evaluate the heating and cooling efficiencies of the normal and overheat FFF processes, temperature profiles of the printed ABS rasters were characterized by using the experimental setup shown in Figure 1. Rectangular prismatic specimens with dimension of 60 × 13 × 3.25 mm were printed at infill angle of [45°/-45°] for the measurement. Each print consisted of 13 layers with a layer thickness of 0.25 mm. Similar to our previous research work (Tran *et al.*, 2022a), the temperature profiles of the polymer rasters were monitored by using a K-type thermocouple connected to a temperature data logger (OMEGA, RDXL6SD-USB). To reduce the heating effects of the build plate on the temperature profile measurement, the thermocouple was embedded at the center of layer 9 (Figure 1a) where its temperature provided by the build plate was below T_g (~84 ^oC) and, therefore, only temperature profiles caused by the deposited ABS melt from layer 10 to layer 13 were measured.

After each of the last 4 layers was deposited and its measurements were recorded, the print was paused for at least 5 minutes to allow the ABS melt to cool down to its stable temperature, named as standby temperature. The diffusion time of the material at layer 9 with the surrounding material was determined by adding the time when its temperature was above T_g after the deposition of each subsequent layer (Tran *et al.*, 2022a).

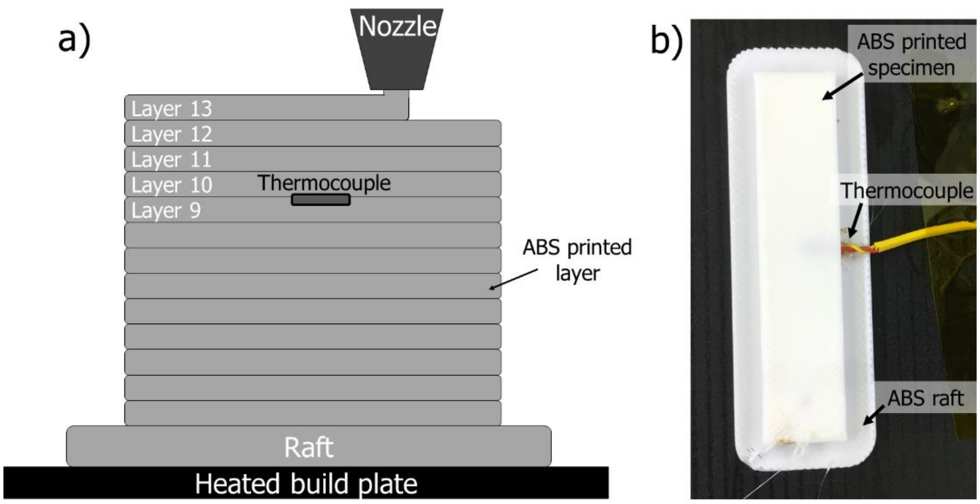

Figure 1. a) Schematic diagram showing experimental setup for temperature profile measurement of ABS printed sample, and b) printed samples with embedded thermocouple.

2.4 Characterization and analysis

Thermogravimetric analysis (TGA, TA Instrument TGAQ500) of the ABS filament was conducted in N_2 from room temperature to 800 °C, with a heating rate of 10 °C/min. Differential scanning calorimetry (DSC, TA Instrument DSCQ200) was performed in Nitrogen from room temperature to 300 °C, with a heating rate of 10 °C/min. Melt flow index (MFI) of the ABS feedstock was measured by using an Instron melt flow tester (CEAST MF20) in accordance to ASTM D1238.

The thickness and width of the printed samples were measured by a Vernier caliper at several positions along their length. The cross-sections and fracture surfaces of the tensile samples were characterized by using a field emission scanning electron microscope (Zeiss UltraPlus FE-SEM) and an optical microscope (Olympus SZ61). Porosity and raster-to-raster weld lengths of the printed samples were determined by analyzing their cross-sections using ImageJ software.

The tensile test of all ABS printed samples was performed by using an Instron static tester (series 5982) equipped with a video extensometer for high accuracy strain measurements. In accordance to ASTM D3039 [34], a total of 24 tensile samples with a dimension of 165 × 13 × 3.25 mm were printed and tested at an elongation rate of 5 mm/min and a gage length of 50 mm. Glass fiber composite tabs and epoxy Araldite® were employed for tabbing with a tab length of 30 mm. The sample stress was calculated by dividing the tensile force by the sample cross-sectional area. For impact test, 40 printed samples in total were characterized by using a Zwick pendulum impact tester (HIT25P) with an impact load of 5.5 J, following ASTM D256-10A.

3. Results and Discussion

3.1 Thermal properties of the ABS filaments

Figure 2a presents TGA results of the ABS filament feedstock. As can be seen, the ABS started to decompose at 385 ^{o}C, suggesting that it was feasible to print the material at temperature as high as 310 ^{o}C. The derived weight curve showed only one single peak at 405 ^{o}C, indicating that the feedstock was highly pure. The weight loss of the ABS samples after the TGA test was 98.69%, corresponding to a residue content of 1.31 wt.%. The residue might be dyes and pigments for polymer coloring and/or additives for improved feedstock printability. The DSC curve shown in Figure 2b indicated that the glass transition temperature (T_g) of the ABS feedstock was approximately 91 ^oC at which the polymer started to be softened for diffusion or entanglement. The MFI of the ABS feedstock at the temperatures used for the printing processes is presented in Figure 2c. As can be observed, the ABS had a MFI of 3.76 g/10min at 250 ^oC, whereas the measurement for 310 ^oC was 23.65 g/10min. The remarkable increase in the MFI (~529%) at increasing temperature indicated that the ABS melt at 310 ^oC had much lower viscosity and, hence, higher flowability than the melt at 250 ^oC.

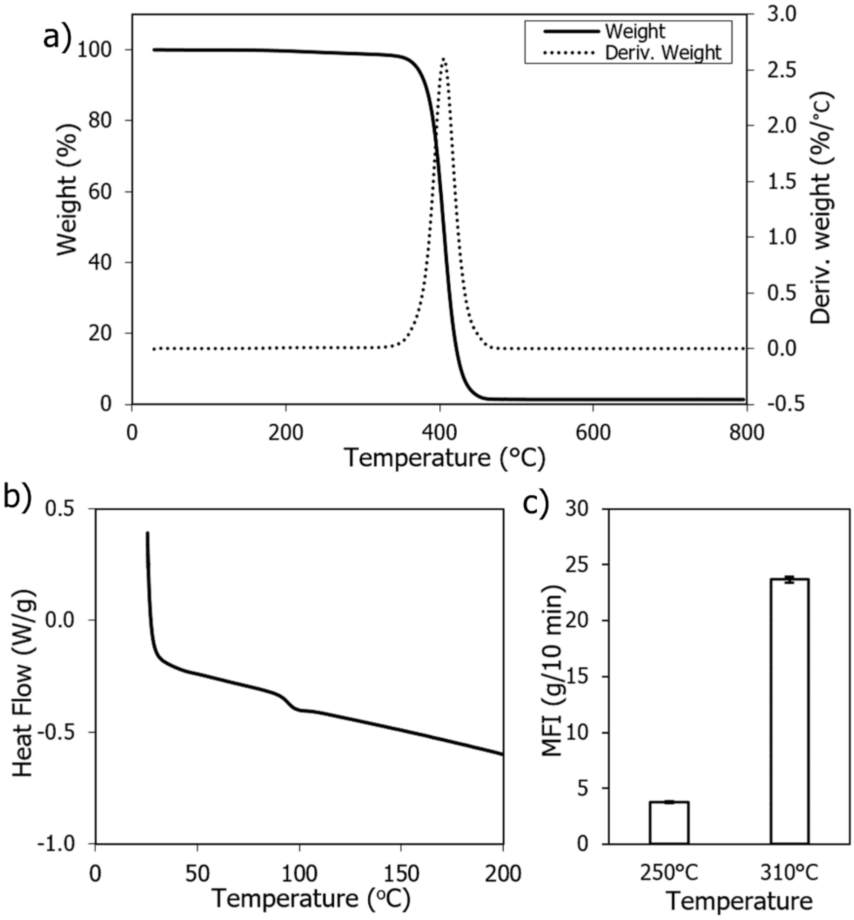

Figure 2. a) TGA results, b) DSC results, and c) MFI results of the ABS feedstock.

3.2 Temperature profiles of the ABS rasters

Figure 3a shows temperature profiles of the material at layer 9 of the printed specimens in the normal and overheat printing processes. As can be seen, although both temperature profiles showed a periodical increase in the temperature of the material at layer 9 after the deposition of each additional layer to the specimen, they possessed different profile patterns. Specifically, the temperature profile of the material at layer 9 in the normal process experienced sharp decreases even below the standby temperatures before and after its peak temperatures during the deposition of the other four ABS layers. These two sudden drops in the temperature at each peak were mainly due to the cooling effects of the fan used in the normal printing process when the extrusion head moved toward the center position of the specimen. Since the cooling fan was not employed in the overheat printing process, the profile patterns at each peak showed a significant increase followed by a more gradual decreasing trend during the deposition of the overheated ABS melt.

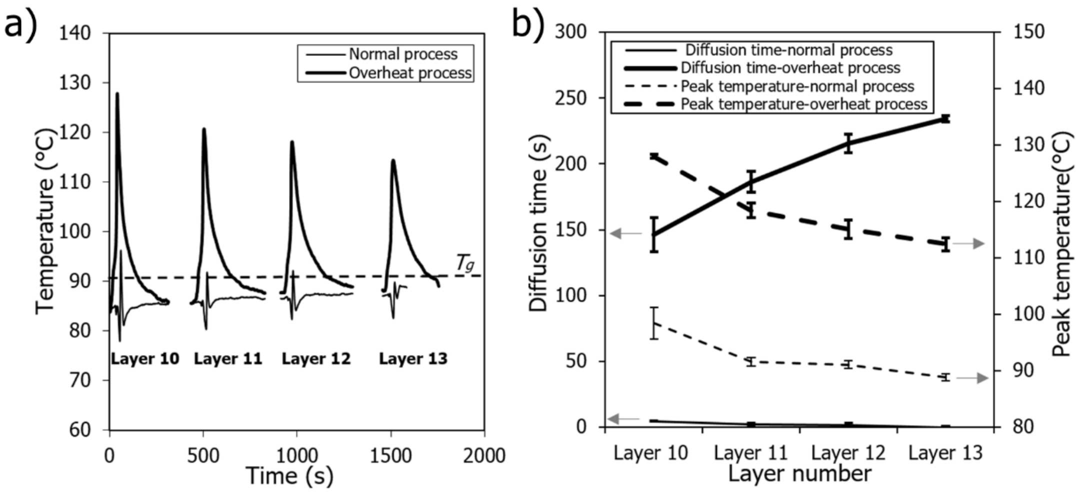

Figure 3. a) Temperature profiles and b) diffusion time and peak temperature of the material at layer 9 ABS during the normal and overheat printing processes.

Figure 3b presents diffusion time and peak temperature of the material at layer 9 during the normal and overheat printing processes. As can be observed, both processes showed a gradual decrease in the peak temperature obtained after each layer deposition. In particular, when the ABS melt was deposited from layer 10 to layer 13, the peak temperature reduced from 98.4 to 88.8 ^{o}C for the normal process and from 128.0 to 112.4 ^{o}C for the overheat process. This decreasing trend could be explained by the lower heat transfer efficiency between the deposited ABS melt to the material at layer 9 with increasing deposited layer number. Since more ABS material was deposited above the material at layer 9 at the higher deposited layer number, it acted as an insulator to reduce the heat transfer efficiency between the materials at layer 9 and the subsequent deposited layers. Additionally, the longer distance between the heat source (freshly deposited material) at the higher deposited layer number and the material at layer 9 increased heat loss, contributing to the reducing trend in the peak temperature of both printing processes. Notably, all peak temperatures in the overheat printing process were considerably higher than those in the normal process thanks to their higher printing temperature and cooling fan turnoff.

Regarding the diffusion time, the normal process exhibited a downward trend from 4.7 to 1.7 s when deposited layer number increased from 10 to 12. At the deposition of layer 13, the peak temperature of the material at layer 9 was below T_g, suggesting that thermal energy provided by the extruded ABS melt at layer 13 was insufficient for the diffusion process of the material at layer 9. The total diffusion time of the material at layer 9 in the normal process was only 8.3 s, which was too short for its complete diffusion and entanglement with the surrounding material. In contrast, the diffusion time in the overheat process showed a gradual increase from 146.3 s for layer 10 to 234.3 s for layer 13, leading to a total diffusion time of 782 s for the material at layer 9. This significantly high diffusion time suggests that the overheat process could offer better polymer diffusion and entanglement between the ABS rasters compared to those fabricated by the normal process.

3.3 Cross-sections and mesostructures of the ABS printed parts

Figures 4 a-d present the cross-sections of the ABS samples printed by the normal and overheat processes at infill angles of [45°/-45°] and [0°/90°]. As can be seen, the internal structure of the printed parts could be classified into 3 main regions: bottom, side, and middle & top. The two side regions of the printed parts had dense structures since the infill overlap of

5% was applied to provide good bonding between the infill and shell of the printed parts. The bottom region (first 5-6 layers) also possessed highly dense structure because the material at this region was always heated at high temperature (~T_g) by the build plate and densified by the mass accumulation and extrusion pressure of the subsequent deposited layers. Conversely, the middle & top region was the least dense with many voids and gaps observed. As the heating effects of the build plate reduced with increasing layer number, void sizes in the middle & top region tended to be larger than those in the bottom region. This is a common issue of specimens printed by low-cost FFF printers equipped with only a heated build plate (Quelho de Macedo *et al.*, 2019).

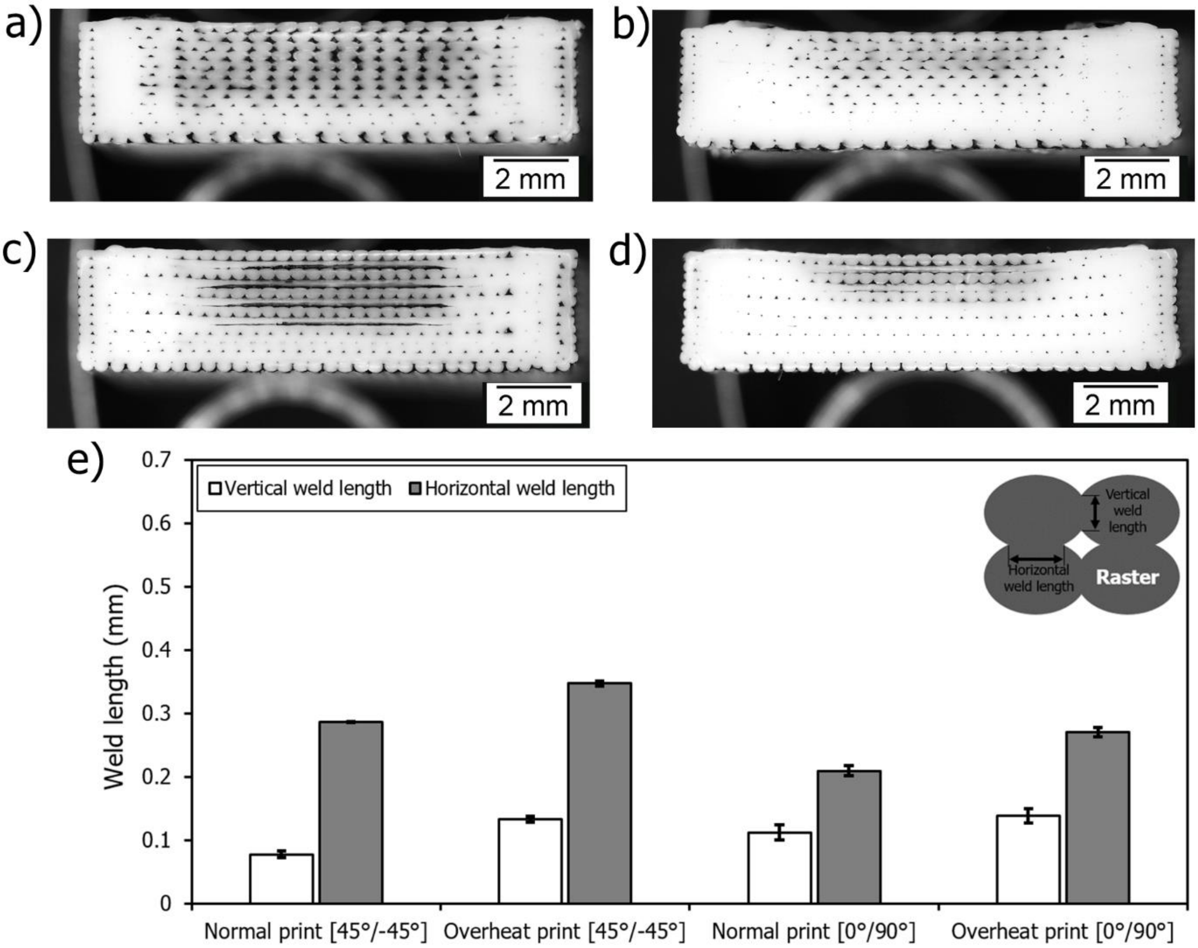

Figure 4. Cross sections of the ABS specimens printed by a) normal process with infill angle of [45°/-45°], b) overheat process with infill angle of [45°/-45°], c) normal process with infill angle of [0°/90°], d) overheat process with infill angle of [0°/90°], and e) Raster-to-raster weld lengths of specimens printed by the normal and overheat processes.

As can be observed, the ABS samples printed by the normal process had many voids and gaps formed between the deposited rasters with porosity of approximately 6.29% for infill angle of [45°/-45°] and 6.63% for infill angle of [0°/90°]. By using the overheat printing process, the porosity of the [45°/-45°] and [0°/-90°] samples reduced to only 1.34% and 1.35%, corresponding to a decrease of 78.69 and 79.64%, respectively. This impressive reduction in porosity might stem from the lower melt viscosity and the prolonged diffusion time of the rasters in the overheat printing process (Tran *et al.*, 2022a; Sun *et al.*, 2008), leading to better polymer diffusion and the formation of lesser pores and voids as well as larger side and bottom dense regions.

Figure 4e compares the weld lengths formed between the adjacent rasters in the middle & top regions of the printed specimens. As can be seen, the overheat printed samples possessed longer weld lengths in all regions compared to their normal printed counterparts. Specifically, the vertical weld lengths in the middle & top region of the [45°/-45°] and [0°/90°] parts printed by the normal process were 0.08 and 0.11 mm, respectively. By using the overheat process, longer vertical weld lengths could be produced with a length of 0.13 mm for infill angle of [45°/-45°] and 0.14 mm for infill angle of [0°/90°]. Similarly, the horizontal weld lengths of the overheat printed parts with infill angles of [45°/-45°] and [0°/90°] were 0.35 and 0.27 mm, correspondingly, which were 20.69 and 28.57% longer than those of the normal printed parts. The increase in the weld lengths of the overheat printed parts was mainly due to the lower viscosity of the ABS melt and longer diffusion process (Abbott *et al.*, 2018; Sun *et al.*, 2008). These results suggested that the overheat process could enhance the structures of the printed part with better bonding quality.

3.4 Tensile and impact properties of the ABS printed parts

Figure 5 presents stress-strain curve, fractured samples, and tensile and impact properties of the ABS specimens printed by different processess. As can be seen, all tensile samples broke within the gage length, indicating that all tensile tests were valid. The ABS parts printed by the normal process at infill angle of [45°/-45°] possessed a tensile strength of 26.99 MPa and a Young's modulus of 1.71 GPa. However, the overheat printed parts with the same infill angle exhibited better tensile performance with 9.15% higher strength and 11.70 % higher Young's modulus. The better tensile performance of the overheat printed parts with infill angle of [45°/-45°] mainly stemmed from their denser internal structure and, thus, better load transfer efficiency between the polymer rasters (Abbott *et al.*, 2018; Sun *et al.*, 2008).

Compared to the [45°/-45°] samples printed by the normal process, the [0°/90°] parts printed by the same process had better tensile performance with a tensile strength of 30.68 MPa and a Young's modulus of 1.97 GPa. Interestingly, the overheat printing process had no remarkable effects on the tensile strength and Young's modulus of the [0°/90°] parts, as observed in Figure 5c. However, with the improvements in the tensile strength and Young's modulus of the overheat printed parts with infill angle of [45°/-45°], the differences between the tensile strength of the parts printed at both infill angles reduced significantly, suggesting that the mechanical performance in the in-plane directions of the ABS parts printed with bidirectional raster structures was more isotropic.

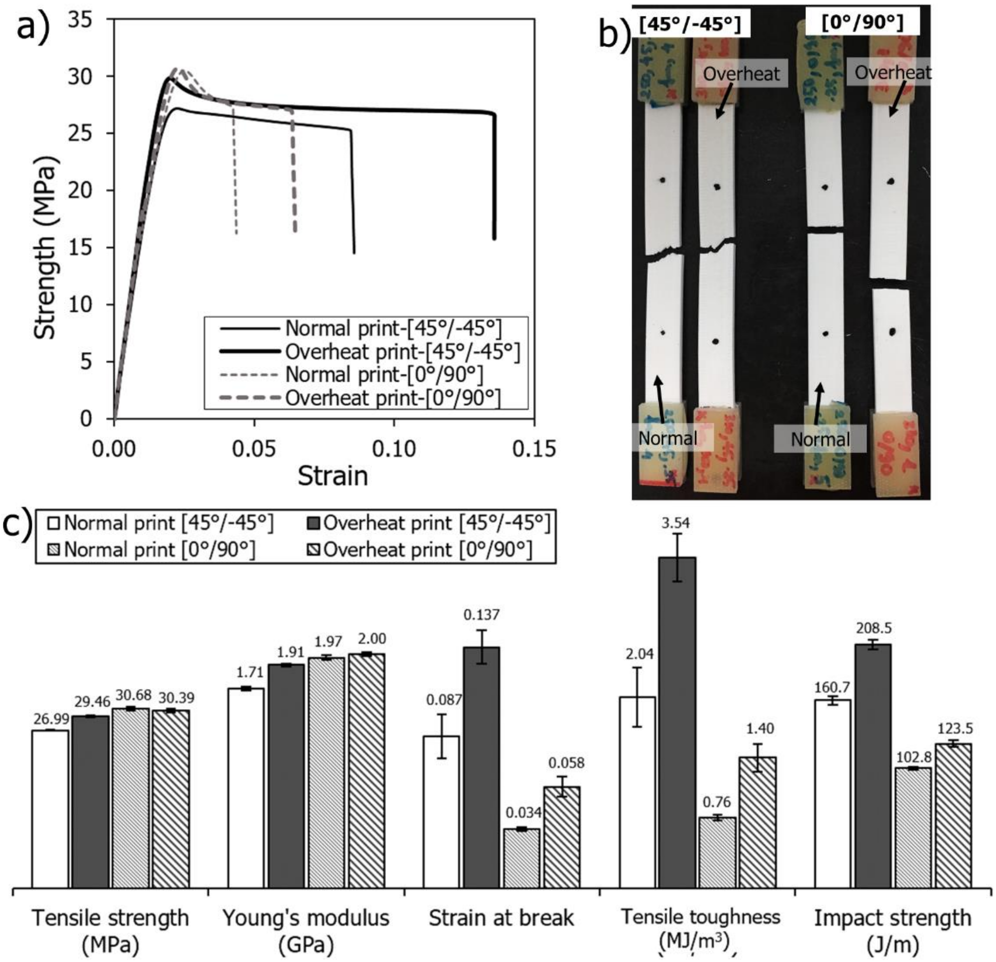

Figure 5. a) Stress-strain curves, b) fractured tensile samples, and c) mechanical properties of ABS part printed by normal and overheat processes.

The mechanical results of the ABS parts printed by the two processess, however, were substantially different in strain at break, tensile toughness, and impact strength. In details, the strain at break of the parts printed by the normal process was 0.087 for infill angle of [45°/-45°] and 0.034 for infill angle of [0°/90°]. By using the overheat printing process, the strain at break at infill angles of [45°/-45°] and [0°/90°] could reach 0.137 and 0.058, corresponding to an enhancement of 57.47 and 70.59%, respectively. Similarly, the tensile toughnesses of the [45°/-45°] and [0°/90°] samples printed by the normal process were 2.04 and 0.76 MJ/m^3, respectively. The overheated samples, however, had much better tensile toughness with 73.53% higher for infill angle of [45°/-45°] and 84.21% higher for infill angle of [0°/90°]. Regarding the impact strength, improvements of up to 29.74% for the [45°/-45°] samples and 20.14% for the [0°/90°] samples were achieved when employing the overheat printing process, reaching 208.5 and 123.5 J/m, respectively. These impressive enhancements could be explained by the better internal structures of the overheat printed parts, suggesting that the FFF overheat printing is an effective method to improve the strain at break, tensile toughness, and impact strength of the ABS printed parts.

Figure 6 shows fracture surfaces of the ABS printed samples after the mechanical tests. Since the samples from both impact and tensile tests had similar failure morphologies, the following analysis and discussion were applicable to both types of loading. As can be seen, there is a gradient of consolidation rate in all SEM samples with better consolidation at the bottom region. All samples printed at infill angle of [0°/90°] exhibited a planar failure (Figures 6a and b) with larger consolidation region observed for the overheat printed samples. The failure mechanisms transitioned from failure akin to bulk polymer at bottom region (higher density) to a mixture of trans-raster and inter-raster at middle region (intermediate consolidation) and finally isolated raster failure at the top region (lower density). This trans-raster failure was characterized by failure iniation at weld points from the two adjacent layers and propagation inwards to the raster meeting in a cusp in the middle of the raster.

For the samples printed at infill angle of [45°/-45°], a planar fracture surface was observed in the bottom region of the overheat specimen (higher density) (Figures 6c and d). Within these areas, no periodicity of the failure patterns was observed, indicating that failure mechanisms akin to those observed in bulk polymers were predominant. Conversely, as the consolidation decreased with increasing layer number, planar failure transitioned to multiplanar serrated failure dominated by the infill directions. In this type of failure, a mixture of trans-raster and inter-raster failure was observed. Both the inter-raster and the trans-raster failure presented a mixed-mode type of failure with component. At this stage, failure could be seen to have initiated at the weld points with the adjacent rasters/layers. As a result of the different stress concentration factors that arose with the different vertical and horizontal weld length, the mechanisms of failure varied with the degree of consolidation.

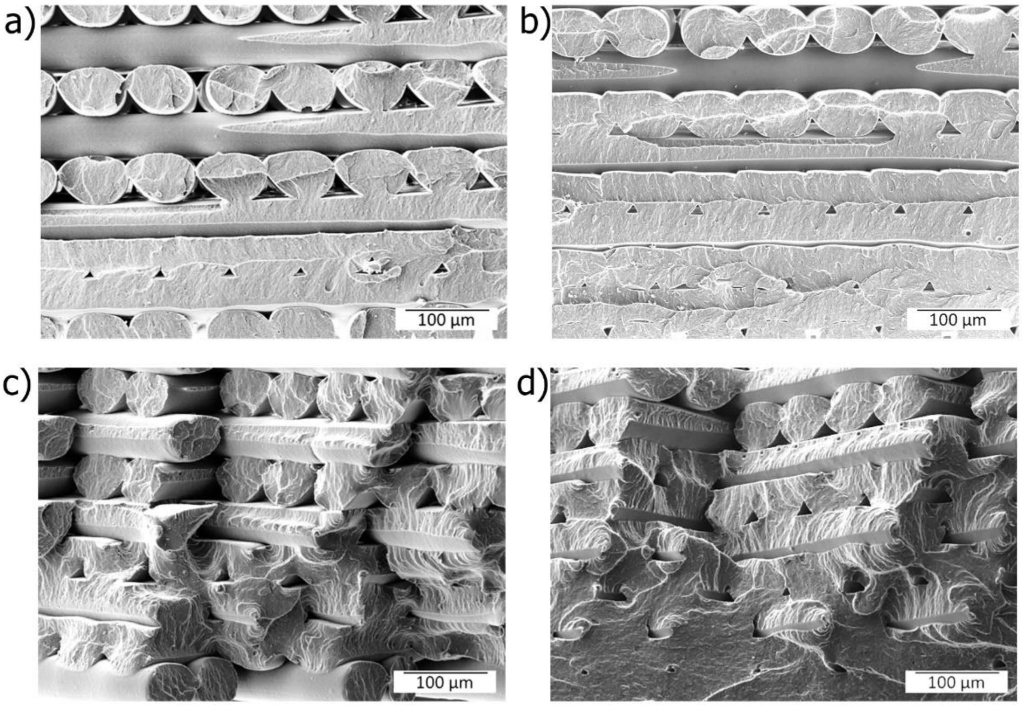

Figure 6. Representative SEM images showing facture surfaces of the impact and tensile samples printed by a) normal process with infill angle of [0°/90°], b) overheat process with infill angle of [0°/90°], c) normal process with infill angle of [45°/-45°], and d) overheat process with infill angle of [45°/-45°].

3.5 Advantages of the overheat printing method for porosity reduction

Figure 7 compares the achieved porosity and porosity reduction percentage for FFF printed parts produced by different process modification and post-treatment methods, such as combination of adding expandable microsphere and annealing (Wang *et al.*, 2016) and modification of extruder with adjustable heat block (Böhler *et al.*, 2020), pre-&post-heating block (Ravoori *et al.*, 2019), pressing roller (Majid *et al.*, 2017), or vibration motor (Keleş *et al.*, 2018). As can be observed, the achieved porosity of the overheat printed ABS parts in this study is comparable to that of cellulose acetate parts printed by the modified extruder with adjustable heat block and about 5 – 9 times lower than that of those fabricated by the other methods. Moreover, the developed overheat printing method could reduce the printed parts' porosity by up to 80%, which is in the range achieved by the method using modified extruder with adjustable heat block but much better than the other reported methods. Another advantage of our developed method is that it is more facile and cost-effective with no requirements of extruder modification and/or additional post-treatment steps. In fact, the developed overheat FFF printing process offers a distinct potential to fabricate highly dense polymer parts with reliable mechanical performance.

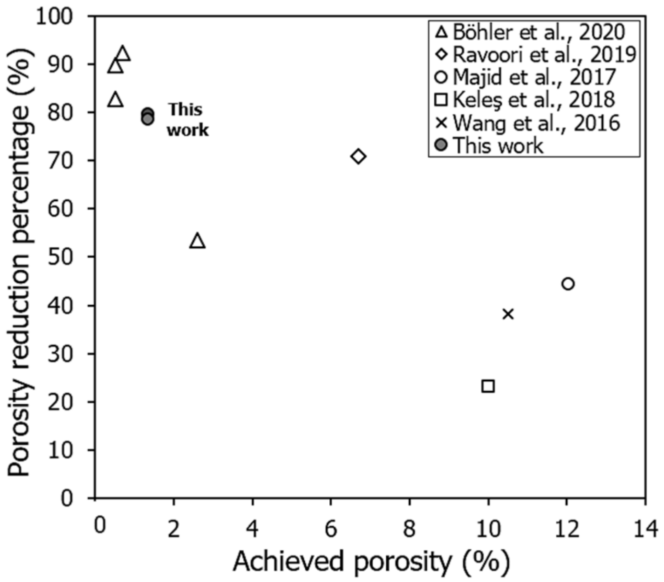

Figure 7. a) Achieved porosity and porosity reduction percentage of FFF printed parts achieved by different methods.

4. Conclusions

In summary, highly dense ABS specimens were successfully fabricated by the overheat FFF printing process. By employing significantly high printing temperature while turning off the cooling fan, the viscosity and cooling rate of the extruded ABS melt reduced remarkably, leading to improved polymer diffusion between the ABS rasters. Consequently, the porosity of the printed parts could decrease by approximately 80% while their raster-to-raster weld lengths increased by up to 62.5%. More importantly, the overheat FFF printed specimens exhibited an improvement of up to 70% in tensile strain at break, 84% in tensile toughness, and 30% in impact strength compared to those fabricated by the normal process. This work demonstrates that our facile but effective overheat printing process has great potential to fabricate high-performance ABS parts for end-use applications.

Reference

Abbott, A. C., Tandon, G. P., Bradford, R. L., Koerner, H. and Baur, J. W. (2018), "Process-structure-property effects on ABS bond strength in fused filament fabrication", *Additive Manufacturing,* Vol. 19, pp. 29-38.

Ahmed, N. A. and Page, J. R. (2013), "Manufacture of an Unmanned Aerial Vehicle (UAV) for Advanced Project Design Using 3D Printing Technology", *Applied Mechanics and Materials,* Vol. 397-400, pp. 970-980.

Böhler, S., Bartel, M., Bohn, A., Jacob, R., Ganster, J., Büsse, T. and Balko, J. (2020), "Highly dense cellulose acetate specimens with superior mechanical properties produced by fused filament fabrication", *Polymer,* Vol. 194, p. 122388.

Grimmelsmann, N., Kreuziger, M., Korger, M., Meissner, H. and Ehrmann, A. (2018), "Adhesion of 3D printed material on textile substrates", *Rapid Prototyping Journal,* Vol. 24 No. 1, pp. 166-170.

Jo, W., Kwon, O. C. and Moon, M. W. (2018), "Investigation of influence of heat treatment on mechanical strength of FDM printed 3D objects", *Rapid Prototyping Journal,* Vol. 24 No. 3, pp. 637-644.

Keleş, Ö., Anderson, E. H. and Huynh, J. (2018), "Mechanical reliability of short carbon fiber reinforced ABS produced via vibration assisted fused deposition modeling", *Rapid Prototyping Journal,* Vol. 24 No. 9, pp. 1572-1578.

Khorasani, M., Loy, J., Ghasemi, A. H., Sharabian, E., Leary, M., Mirafzal, H., Cochrane, P., Rolfe, B. and Gibson, I. (2022), "A review of Industry 4.0 and additive manufacturing synergy", *Rapid Prototyping Journal,* Vol. ahead-of-print No. ahead-of-print.

Kuo, C. C., Chen, J. Y. and Chang, Y. H. (2021), "Optimization of Process Parameters for Fabricating Polylactic Acid Filaments Using Design of Experiments Approach", *Polymers,* Vol. 13 No. 8, p. 1222.

Kuznetsov, V. E., Solonin, A. N., Tavitov, A., Urzhumtsev, O. and Vakulik, A. (2020), "Increasing strength of FFF three-dimensional printed parts by influencing on temperature-related parameters of the process", *Rapid Prototyping Journal,* Vol. 26 No. 1, pp. 107-121.

Lathers, S. and La Belle, J. (2017), "Additive Manufactured Biomimicking Actuator with Shape Memory Polymer Composite for Prosthetic Actuators", *3D Printing and Additive Manufacturing,* Vol. 4 No. 4, pp. 201-213.

Majid, S. N. A., Alkahari, M. R., Ramli, F. R., Maidin, S., Fai, T. C. and Sudin, M. N. (2017), "Influence of Integrated Pressing during Fused Filament Fabrication on Tensile Strength and Porosity", *Journal of Mechanical Engineering,* Vol. SI 3 No. 2, pp. 185-197.

Quelho de Macedo, R., Ferreira, R. T. L. and Jayachandran, K. (2019), "Determination of mechanical properties of FFF 3D printed material by assessing void volume fraction, cooling rate and residual thermal stresses", *Rapid Prototyping Journal,* Vol. 25 No. 10, pp. 1661-1683.

Ravoori, D., Prajapati, H., Talluru, V., Adnan, A. and Jain, A. (2019), "Nozzle-integrated pre-deposition and post-deposition heating of previously deposited layers in polymer extrusion based additive manufacturing", *Additive Manufacturing,* Vol. 28, pp. 719-726.

Schirmeister, C. G., Hees, T., Licht, E. H. and Mülhaupt, R. (2019), "3D printing of high density polyethylene by fused filament fabrication", *Additive Manufacturing,* Vol. 28, pp. 152-159.

Sun, Q., Rizvi, G. M., Bellehumeur, C. T. and Gu, P. (2008), "Effect of processing conditions on the bonding quality of FDM polymer filaments", *Rapid Prototyping Journal,* Vol. 14 No. 2, pp. 72-80.

Tran, T. Q., Canturri, C., Deng, X., Tham, C. L. and Ng, F. L. (2022a), "Enhanced tensile strength of acrylonitrile butadiene styrene composite specimens fabricated by overheat fused filament fabrication printing", *Composites Part B: Engineering,* Vol. 235, p. 109783.

Tran, T. Q., Chinnappan, A., Lee, J. K., Loc, N. H., Tran, L. T., Wang, G., Kumar, V. V., Jayathilaka, W. A. D. M., Ji, D., Doddamani, M. and Ramakrishna, S. (2019), "3D Printing of Highly Pure Copper", *Metals,* Vol. 9 No. 7, p. 756.

Tran, T. Q., Ng, F. L., Kai, J. T. Y., Feih, S. and Nai, M. L. S. (2022b), "Tensile Strength Enhancement of Fused Filament Fabrication Printed Parts: A Review of Process Improvement Approaches and Respective Impact", *Additive Manufacturing,* Vol. 54, p. 102724.

Wang, J., Xie, H., Weng, Z., Senthil, T. and Wu, L. (2016), "A novel approach to improve mechanical properties of parts fabricated by fused deposition modeling", *Materials & Design,* Vol. 105, pp. 152-159.

Wang, X., Zhao, L., Fuh, J. Y. and Lee, H. P. (2019), "Effect of Porosity on Mechanical Properties of 3D Printed Polymers: Experiments and Micromechanical Modeling Based on X-ray Computed Tomography Analysis", *Polymers,* Vol. 11 No. 7, p. 1154.

Wiese, M., Thiede, S. and Herrmann, C. (2020), "Rapid manufacturing of automotive polymer series parts: A systematic review of processes, materials and challenges", *Additive Manufacturing,* Vol. 36 No., p. 101582.

Zhang, Y., Poli, L., Garratt, E., Foster, S. and Roch, A. (2020), "Utilizing Fused Filament Fabrication for Printing Iron Cores for Electrical Devices", *3D Printing and Additive Manufacturing*, Vol. 7 No. 6, pp. 279-287.